10554 *J. Phys. Chem. A* **2005,** *109,* 10554−10562

Kinetics of Metal Organic−Ammonia Adduct Decomposition: Implications for Group-III Nitride MOCVD

J. Randall Creighton* and George T. Wang

Sandia National Laboratories, P.O. Box 5800, MS-0601, Albuquerque, New Mexico 87185

Received: August 5, 2005; In Final Form: September 20, 2005

We have used infrared spectroscopy to investigate the decomposition of the gas-phase $(Me)_3M{:}NH_3$ (M = Al, Ga, In) adducts from room temperature to 573 K, at reactant concentrations in the nominal range used for Al(Ga,In)N metal organic chemical vapor deposition. At 473−523 K $TMAl{:}NH_3$ decomposes quantitatively to yield $(Me_2)AlNH_2$ and CH_4. Comparison of the experimental and theoretical spectra indicates that the majority of the aluminum metal organic product exists in dimer form, i.e., $[(Me_2)AlNH_2]_2$. The decomposition reaction exhibits unimolecular decomposition kinetics with rate constant parameters of $\nu = 1 \times 10^{12}\ s^{-1}$ and $E_a = 25.7$ kcal/mol. At temperatures <543 K, TMGa + NH_3 and TMIn + NH_3 mixtures are dominated by reversible adduct formation−dissociation with no detectable quantities of CH_4 produced. At 574 K a small amount of decomposition is observed in TMGa + NH_3 mixtures, which can be explained by a simple kinetic model that includes the effect of adduct equilibrium. Results demonstrate that the $(Me)_3Al{:}NH_3$ decomposition rate is fast enough to contribute to the early stages of a concerted parasitic chemical reaction mechanism, but the $(Me)_3Ga{:}NH_3$ decomposition rate is too slow.

1. Introduction

Metal organic chemical vapor deposition (MOCVD) is the dominant method of depositing AlN, GaN, and AlGaInN alloy semiconductor thin films.[1] The method almost always involves reacting the group-III metal organics, trimethylaluminum (TMAl), trimethylgallium (TMGa), and/or trimethylindium (TMIn) with ammonia. Unfortunately, the high temperatures (1000−1400 K) required to deposit high-quality material can also lead to the initiation of a sequence of gas-phase parasitic chemical reactions.[2−10] These reactions may ultimately lead to nanoparticle formation that can consume a significant fraction of the group-III growth precursor.[6−9] This loss of growth precursor produces temperature-dependent thin film growth rates under conditions that are normally mass-transport limited. The parasitic reactions also cause the growth rates and alloy compositions to vary nonlinearly with precursor concentration. All of these effects generally make it much harder to control and reproduce the MOCVD process. Our ability to understand and model these chemical processes should lead to improvements in reactor design and operational conditions.

As previously reported, these parasitic chemical reactions lead to formation of gas-phase nanoparticles,[7−9] which are suspended away from the growing film by a thermophoretic force. These nanoparticles represent the end product of a sequence of gas-phase nucleation and particle growth reactions that are still not well understood. Any attempt to understand the parasitic chemical mechanism must account for adduct formation reactions between NH_3 and TMAl, TMGa, or TMIn, as in reaction 1.

$$(Me)_3M + NH_3 \leftrightarrow (Me)_3M{:}NH_3 \quad \text{reversible adduct formation (M = Al, Ga, In)} \quad (1)$$

$$(Me)_3M{:}NH_3 \rightarrow CH_4 + (Me)_2M{-}NH_2 \quad \text{methane elimination, amide formation} \quad (2)$$

$$[(Me)_2M{-}NH_2]_n + (Me)_2M{-}NH_2 \leftrightarrow [(Me)_2M{-}NH_2]_{n+1} \quad \text{association reactions } (n = 1, 2, ...) \quad (3)$$

Formation of the group-III/ammonia adduct, $(CH_3)_3M{:}NH_3$, appears inevitable at the point where the gases are mixed in any conventional MOCVD system. Whether or not these reactions represent the first step in the parasitic chemical reaction mechanism is still somewhat controversial and may depend on which group-III element is involved. In some cases (Al, Ga) and conditions, simple physical condensation or homogeneous nucleation of the adduct may occur due to its low vapor pressure.[11] Following adduct formation, a next likely step involves a CH_4 elimination reaction (see reaction 2), forming the $(CH_3)_2M{-}NH_2$ species (sometimes referred to as an "amide"[12]). Oligomerization and further CH_4 elimination and could initiate particle nucleation, although a detailed understanding of these latter steps is lacking. We will refer to this pathway as the "amide", or concerted parasitic chemical, mechanism.

Another scenario is that reactions 2 and 3 (and subsequent related steps) are not fast enough to be significant, and simple pyrolysis of the precursors at high temperatures is the driver for particle nucleation. There is much qualitative and quantitative evidence suggesting that the AlN chemistry is dominated by the "amide", or concerted pathway, while the GaN and InN chemistry is dominated by the "radical" pathway.[9] One goal of this paper is to put this assertion on a more quantitative basis by measuring the kinetics of the gas-phase adduct dissociation step, reaction 2. A previous paper reported the adduct equilibrium constants for TMGa and TMIn.[13]

Much of what is known regarding the adduct chemistry involves solid, liquid, or solution studies of the Al and Ga precursors. In the case of solid $(Me)_3Al{:}NH_3$, methane elimination begins at the melting point (∼328 K) and is complete at

---

* Corresponding author. E-mail: jrcreig@sandia.gov.

10.1021/jp054380s CCC: $30.25

~343 K.[12] A second decomposition step begins at the amide melting point (~413 K). $(Me)_3Ga:NH_3$ exhibits very similar chemistry, evolving the first methane at 343−393 K and forming the amide, $(Me)_2Ga-NH_2$.[14,15] Heating this product above 413 K also initiates further methane evolution.[14] Using these observations to infer what happens in the gas-phase MOCVD environment may not be straightforward. Catalyzed[16] and higher order mechanisms available in the condensed phase may not be viable in the gas phase due to much lower densities. The time scales of the two environments are also considerably different. Most of the condensed phase observations were done in a batch mode, over a period of minutes to hours, while the MOCVD process in done in a flowing gas stream with residence times of a few seconds or less.

We have recently shown, using IR spectroscopy, that at ~520 K the $TMAl:NH_3$ adduct is completely converted into gas-phase $(CH_3)_2AlNH_2$ at nominal MOCVD concentrations, pressures (50−200 Torr), and residence times.[9] The results for the $(Me)_3Ga-NH_3$ adduct are more varied and controversial. Using a flow tube reactor with mass spectrometer detection, Thon and Kuech[17] reported that the $(Me)_3Ga:NH_3$ adduct decomposes quantitatively at "an extremely high rate" at $T > 423$ K for the gas-phase conditions they studied (76 Torr). We note that they report no $(CH_3)_xGaNH_y$ ions in the mass spectrum for the amide. Schäfer et al.[18] used mass spectroscopy in a flow system (30 Torr) with sampling through a heated substrate and detected some signals attributed to the amide dimer, i.e., $[(CH_3)_2GaNH_2]_2$, in the 300−523 K range, although the intensities were very small relative to the original TMGa signal. Bergmann et al.[19] also used mass spectrometric sampling of a flow tube reactor (20 Torr, 100 ms residence time) and detected similar ions related to the amide dimer but also at intensities less than 1/100 of the initial TMGa signal. In our previous work using IR spectroscopy as the diagnostic[9,13] we found no measurable CH_4 formation in $TMGa + NH_3$ mixtures below 543 K, with a minimum CH_4 detection limit of ~0.5% TMGa decomposition. Several other IR observations of the gas-phase $(Me)_3Ga:NH_3$ adduct have been,[20−22] but the kinetics of adduct decomposition or dissociation were not ascertained. Much less is known about the $TMIn-NH_3$ adduct chemistry, although our previous work was similar to our $TMGa-NH_3$ findings, no measurable CH_4 at temperatures below 543 K.[9,13]

Several groups have investigated the relevant adduct and amide chemistry using quantum chemical calculations, in particular with density functional theory (DFT).[23−29] In many cases transition states where calculated for unimolecular decomposition of the adducts. Mihopoulos et al.[6] constructed an AlN MOCVD mechanism using the calculated (and estimated) rate constants for reactions 1−3 that reproduced many of the unusual MOCVD features observed experimentally.

For $(Me)_3Ga:NH_3$ the calculated activation energies are in the range of 30−34 kcal/mol, which when combined with calculated or estimated values for the preexponential factors[6,23,29] can be used to determine the unimolecular decomposition rate constant. The results generally yield rate constants that are much too small to be consistent with the Thon and Kuech observation. Some have questioned whether the amide pathway is in fact viable or important for GaN MOCVD.[9,29] Using DFT, more complex bimolecular pathways for $(Me)_3Ga:NH_3$ decomposition have been found with substantially lower activation energies,[23,25,27] but it is not known if the overall rates for such processes are significant at MOCVD conditions.

In this paper we examine the kinetic details of reaction 2 for the aluminum species. We also more closely analyze the vibrational modes of the product and determine the degree of association. In contrast to our earlier assignment[9] the aminodimethylalane (dimethylaluminum amide) species is found to dimerize under the conditions of study. While the irreversible decomposition reaction of the $TMAl:NH_3$ adduct was easily observable, evidence for the analogous pathway for $TMGa:NH_3$ and $TMIn:NH_3$ was only found at the very highest temperature. The results for $TMGa:NH_3$ are consistent with a simple model that includes the effect of the adduct equilibrium and the estimated rate constant for decomposition. Extrapolation of this model for TMGa to higher temperatures shows that the *radical* pathway is far more important that the *amide* pathway for MOCVD conditions. Experimental results for TMIn are largely masked by a decomposition reaction that occurs even in the absence of NH_3.

2. Experimental and Theoretical Procedure

Gas-phase infrared spectroscopy was performed with a Mattson RS-1 FTIR spectrometer at 2 cm^{-1} resolution. A heatable long path length gas cell was mounted in the sample compartment of the instrument, which has been previously described.[13] Briefly, the IR beam enters and exits through a single KCl window (6 mm thickness) and is folded once with a Au-coated spherical mirror ($r = 40.6$ cm), giving an internal path length of ~80 cm. This intermediate value of path length gives a reasonable absorbance for the organometallic precursors and adducts without producing an excessive absorbance from the gas-phase NH_3 (which is 200−800× higher in concentration). In all spectra shown for $(Me)_3M + NH_3$ mixtures, the very large NH_3 spectrum has been removed for clarity. The cell could be heated to ~575 K, with the upper temperature limit determined by the thermal properties of the fluorocarbon-based elastomeric O-ring used on the KCl window seal. The temperature was measured at several points internally, and the uniformity was <5 K (typically <3 K). The gas cell was connected in parallel with our research MOCVD reactor and operated at flow rates and pressures in the same nominal range used for AlGaInN deposition. Gases were mixed upstream before injection into the cell, with concentrations kept below the onset of adduct condensation.[11] A long internal gas inlet tube allowed the gases to preheat before they were fully introduced into the cell. The residence time in this internal tube is ~600× smaller that the main cell residence time, so it represents a very small perturbation to the kinetic analysis.

The total pressure was varied from 50 to 200 Torr, with a total flow rate of 6.5 slm. For this flow rate, at 300 K and 100 Torr total pressure, the mean residence time in the cell is 3.54 s (internal volume = 3.2 L). Hydrogen was used as the carrier gas. The ammonia flow rate for most experiments was fixed at 1.0 slm, giving $P(NH_3) = 15.4$ Torr at the 100 Torr total pressure condition. TMAl, TMGa, and TMIn were delivered using a standard bubbler configuration to give $P(\text{TMAl-monomer}) = 23.5$ mTorr, $P(\text{TMGa}) = 62.8$ mTorr, and $P(\text{TMIn}) = 20.3$ mTorr at the 100 Torr total pressure condition. The partial pressure of the reactants scales with total pressure, so at 200 Torr the values are double the 100 Torr values given above. We note that there are some variations in the reported vapor pressure curves for TMAl and especially TMIn, which can affect the quantitative analysis of the decomposition products. We use the TMAl curve from ref 30, the TMGa curve from ref 31, and the TMIn curve from ref 32. We also assume that TMAl is 100% dimerized at the bubbler conditions and give flow rates and partial pressures on a TMAl monomer basis. Methane was supplied via a dilution line configuration and used

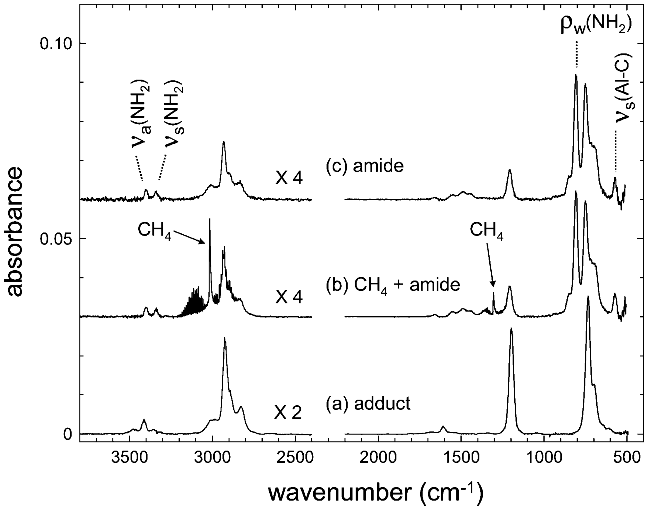

Figure 1. FTIR of TMAl + NH_3 mixture at (a) 372 K, adduct, (b) 541 K, amide + CH_4, and (c) 541 K, pure amide, CH_4 component removed. The NH_3 component has been removed from each spectrum. Conditions are as follows: $P_{NH_3} = 15.4$ Torr; $P_{TMAl} = 23.4$ mTorr (monomer); $P_{total} = 100$ Torr.

for calibration purposes. At room temperature, 100 Torr total pressure, and 6.5 slm total flow rate, the detection limit for CH_4 is about 0.3 mTorr (0.02 sccm).

Main-group chemistry has been widely studied using density functional theory (DFT) methods. DFT calculations using the B3LYP hybrid functional[33] were employed in this study to examine the vibrational frequencies of expected reaction products between NH_3 and the group-III metalorganics. The Gaussian 03 software package[34] was used for all the calculations. Geometry optimizations were carried out without symmetry constraints using the 6-31G(d) basis set to locate the stationary points on the potential energy surface. Frequency calculations using the 6-31G(d) basis set were performed for each stationary point to obtain the zero-point energies, thermal corrections, and infrared frequencies. The calculated stationary points on the potential energy surface were verified by analysis of the normal modes as minima by the presence of no imaginary frequencies. Vibrational spectra were synthesized using the calculated frequencies and intensities, assuming Gaussian line shapes with a 30 cm^{-1} bandwidth. Vibrational frequencies were scaled by 0.96, which is the recommended scaling factor for this basis set.[35] All calculated energies reported in this paper have been zero-point corrected.

3. Results and Discussion

3.1. Infrared Spectroscopy of $(Me)_3Al + NH_3$ Mixtures. Between 298 and 373 K and for the reactant partial pressures studied, the $(Me)_3Al:NH_3$ adduct is rapidly formed and is virtually 100% associated. Near room temperature and slightly above there is also evidence for a 2:1 complex formed for both $(Me)_3Al$ and $(Me)_3Ga$, but this topic is covered in another publication.[36] A number of unique modes appear in $(Me)_3Al:NH_3$ FTIR spectrum (see Figure 1, curve a) that are not attributed to $(Me)_3Al$ (g) or NH_3(g). This adduct spectrum is in good agreement with the reported condensed phase spectra[37] and is discussed in more detail in a previous publication.[9,36] The IR spectrum of the $(Me)_3Al:NH_3$ adduct also shares many qualitative similarities with the spectra for $(Me)_3Ga:NH_3$ and $(Me)_3In:NH_3$.[9] Heating above ~373 K leads to adduct decomposition and the appearance of two new species, CH_4 and $(Me)_2Al-NH_2$ (see Figure 1, curve b). This is in marked contrast to the behavior of the $(Me)_3Ga:NH_3$ and $(Me)_3In:NH_3$ adduct, which undergo *reversible* adduct dissociation up to ~543 K.[13] The $(Me)_3Al:NH_3$ decomposition reaction (i.e. reaction 2) goes to completion in the 473−523 K range, depending on reactor residence time. Removing the methane spectral contribution from the mixture leaves the pure $(Me)_2Al-NH_2$ spectrum (Figure 1, curve c). Compared to the adduct spectrum, the amide has differences in the N−H stretching region and two new modes at 809 and 572 cm^{-1}. We will mainly discuss four characteristic modes, $\nu_a(NH_2)$, $\nu_s(NH_2)$, $\rho_w(NH_2)$, and $\nu_s(AlC_2)$, that (with the aid of DFT calculations) identify this species and determine the degree of association.

We had originally attributed the amide spectrum seen in Figure 1, curve c, as monomeric $(Me)_2Al-NH_2$,[9] on the basis of comparisons to the matrix-isolated monomer results by Müller.[38] The matrix-isolated monomer exhibits an intense ν(Al−N) absorption near 810 cm^{-1}, which is indicative of a strong covalent Al−N bond. For reference, the ν(Al−N) mode in the adduct is at a much lower frequency (383 cm^{-1}),[38] consistent with a much weaker dative bond.[39] The presence of the strong 809 cm^{-1} peak in our gas-phase spectrum previously led us to propose that the observed $(Me)_2Al-NH_2$ species was monomeric. If the species was dimerized or trimerized, the ν(Al−N) mode should be shifted to lower frequency, e.g. 450−600 cm^{-1},[40−43] because of the reduced bond order.[39] However, close comparison of the gas-phase $(Me)_2Al-NH_2$ spectrum with the matrix-isolated results reveals some inconsistencies.

One example is the moderately intense peak at 572 cm^{-1} that is not seen for the matrix-isolated molecule, nor was any nearby mode of significant intensity predicted in Müller's calculations.[38] This peak is in the range expected for a ν(Al−C) mode, which might be sensitive to the degree of association due to large changes in the Al−C bonding geometry. In fact, for the dimer of a related compound, $[(Me)_2AlN(Me)_2]_2$, the ν_s(Al−C) mode appears at 576 cm^{-1}.[44]

The $\nu(NH_2)$ modes in the gas-phase species are also significantly lower than the matrix-isolated monomer (see Table 1). If our measured gas-phase spectrum corresponds to the monomer, then the process of matrix isolation requires a blue-shift of 87 and 70 cm^{-1} for the $\nu_a(NH_2)$ and $\nu_s(NH_2)$ modes. A frequency shift of this magnitude (2.5 and 2.1%) for a stable molecule is highly unlikely,[45] which cast some doubt on the assignment of the gas-phase species being the monomer. Another scenario is that the gas-phase species is another related species but with a different local N−H bonding structure. In the monomeric $(Me)_2Al-NH_2$ molecule a weak π-bond leads to a planar Al−N−H geometry[38,46] and sp^2-hybridized NH bonding. In the dimer (or trimer) the π-bond is absent and NH_2 groups are sp^3-hybridized, which usually exhibits lower ν(N−H) frequencies (compared to sp^2 NH).

While close examination of the ν(N−H) region suggest that the gas-phase species might indeed be associated (e.g. dimeric), this would also lead to a significant downward shift of the ν(Al−N) peak near 810 cm^{-1}, yet we still observe a strong mode at 809 cm^{-1}. For the dimer model to be valid, another mode must be responsible for the strong peak at 809 cm^{-1}. These unresolved questions led us to calculate the vibrational spectra for the monomeric and dimeric $(Me)_2Al-NH_2$ species, which are shown in Figure 2a,b. The dimer spectrum was scaled to approximate the intensity of the 809 cm^{-1} mode. The monomer spectrum used the same dimer scaling factor ×2, to simulate the 2× higher gas-phase molar density.

First, note in Figure 2a and Table 1 that the process of creating a dimer from two monomers does indeed result in a 70−90

TABLE 1: Comparison of Frequencies (cm^{-1}) in the N−H Stretching Region

freq	gas phase (this work)	matrix-isolated monomer[38]	$\Delta\nu$(exp) gas−matrix	DFT dimer	DFT monomer	$\Delta\nu$(DFT) dimer−monomer
$\nu_a(NH_2)$	3400 ± 1	3486.5	−87	3422.3	3506.8	−84.5
$\nu_s(NH_2)$	3341 ± 2	3411.0	−70	3349.2	3421.7	−72.5

cm^{-1} downward shift in the $\nu(NH_2)$ modes. The theoretical dimer spectrum also predicts the $\nu(NH_2)$ frequencies quite well, with deviations of +22 and +8 cm^{-1} for the $\nu_a(NH_2)$ and $\nu_s(NH_2)$ modes, respectively.

The other aspects of the simulated dimer spectrum that more closely resemble the experimental results are apparent in the lower frequency ranges displayed in Figure 2b. A major success of the calculation is the appearance of an intense NH_2 wagging mode, i.e., $\rho_w(NH_2)$, at 821.8 cm^{-1}, which gives us another possible assignment for the 809 cm^{-1} peak observed experimentally. The dimer spectrum also does a better job simulating the relative intensities and shape of the various overlapping $\rho_r(CH_3)$ modes between 680 and 780 cm^{-1}. Finally, the dimer spectrum exhibits a $\nu_s(AlC_2)$ mode at 545.9 cm^{-1}, which can reasonably account for the observed mode at 572 cm^{-1} (−22 cm^{-1} deviation) of similar relative intensity. From the specific results for the $\nu_a(NH_2)$, $\nu_s(NH_2)$, $\rho_w(NH_2)$, and $\nu_s(AlC_2)$ modes and the overall qualitative aspects of the simulated spectra, we conclude that the gas-phase species we observe is in fact the dimer of the amide, i.e., aminodimethylalane, $[(Me)_2AlNH_2]_2$. Although all indications are that the monomer is first formed by reaction 2, dimerization has no reaction barrier and rapidly forms.[6,25] The calculated dimerization energy of −55 kcal/mol (this work) ensures that there is little reversibility in this step at the temperatures studied.

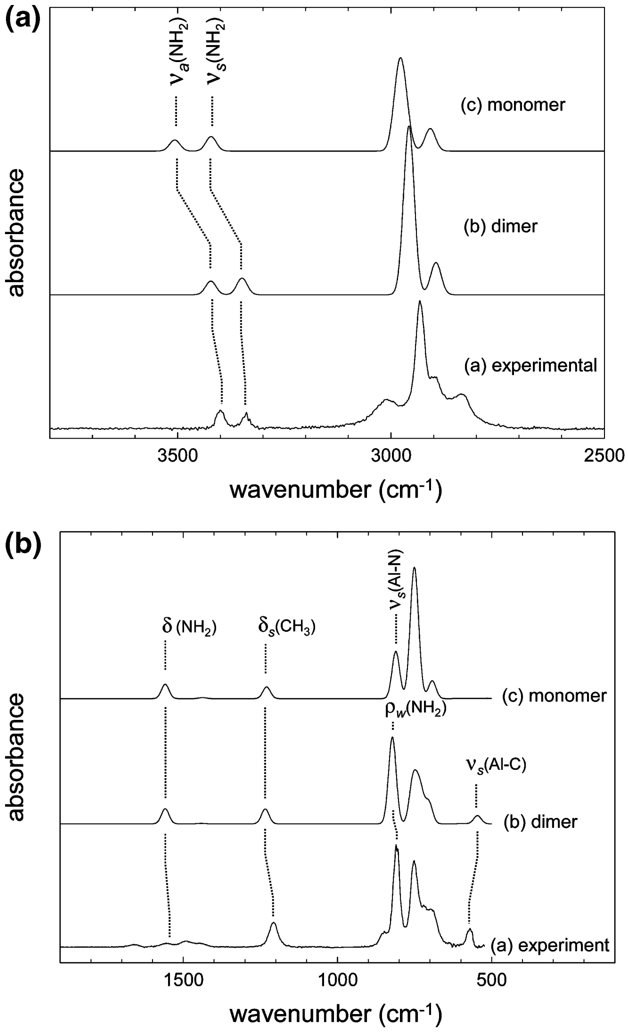

Figure 2. (a) Comparison (high wavenumber range) of the experimental gas-phase IR spectrum (a) with the theoretical spectrum of the dimer (b) and monomer (c). (b) Comparison (low wavenumber range) of the experimental gas-phase IR spectrum (a) with the theoretical spectrum of the dimer (b) and monomer (c).

3.2. Kinetics of $(Me)_2Al-NH_2$ Formation. By measuring the amount of reaction products formed (methane and amide) as a function temperature, concentration, and residence time, we can determine the kinetic order and rate constant parameters (ν, E_a) for the amide formation reaction (i.e. reaction 2). In the case of CH_4 formation, we can put the production rate on a quantitative scale by comparing the measured CH_4 component (e.g. in Figure 1, curve b) to a reference CH_4 spectrum of known mass flow rate. Because of ideal gas expansion and the temperature dependence of the CH_4 rovibrational IR line shapes, a CH_4 reference spectrum was recorded at every condition (temperature, total pressure) we made a kinetic measurement. Measurements of the CH_4 formation rate due to $(Me)_3Al{:}NH_3$ decomposition are shown in Figure 3, as a function of temperature and reactor total pressure. The dashed lines are derived from a simple unimolecular rate expression described later in the text. Under the flow rates and concentrations studied, the reaction becomes detectable at 370−400 K and goes to completion by ~ 540 K. At 541 K the amount of CH_4 produced is 1.41 ± 0.09 sccm, which when compared to the input TMAl flow rate of 1.53 ± 0.15 sccm demonstrates that ~1 mol of CH_4 is produced for every 1 mol of TMAl consumed (within experimental uncertainties). As the temperature is increased (to 584 K) there is a slight rise in CH_4 production, which may be signs of a 2nd decomposition step (vide infra).

We can also measure the degree of reaction progress by monitoring IR mode intensities specific to the amide product. In particular we will use the $\rho_w(NH_2)$ mode intensity as a measure of the amide concentration. Because the gas density drops as $1/T$, for convenience we will convert these concentration measurements to relative partial pressure measurements by multiplying by the absolute temperature; results are shown in

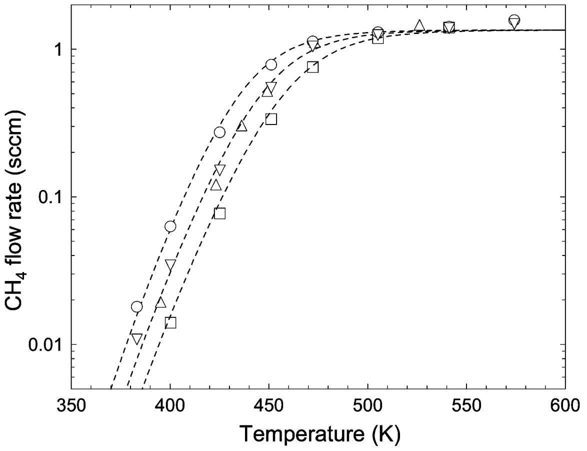

Figure 3. CH_4 formation rate from the TMAl:NH_3 adduct as function of temperature and total pressure: P = 50 (squares), 100 (triangles), and 200 (circles) Torr. Solid curves are generated from a unimolecular rate expression and the measured rate constant (see text).

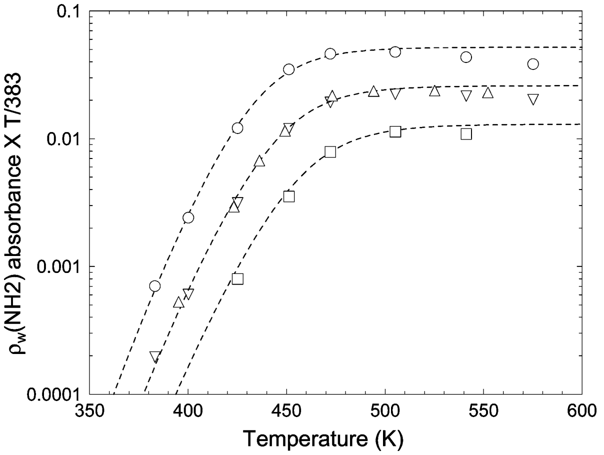

Figure 4. Formation kinetics of measured by the $\rho_w(NH_2)$ mode as function of temperature and total pressure: $P = 50$ (squares), 100 (triangles), and 200 (circles) Torr. Solid curves are generated from a unimolecular rate expression and the measured rate constant (see text).

Figure 4. Unlike the CH_4 measurement method, in this case we are measuring concentration (scaled to give partial pressures) instead of product flow rate, so the final signal levels scale with total pressure. Similar to the CH_4 results, the $\rho_w(NH_2)$ mode intensity measurements exhibit rapid growth from 380 to 480 K and reach saturation around 510−540 K. In this case the signals begin to decrease slightly above 540 K, which might be another sign of the onset of a 2nd decomposition step (vide infra).

To extract quantitative kinetic information from these results we will assume that continuous-flow stirred tank reactor (CSTR) conditions apply. This should be a good assumption given the relatively low total pressures and high diffusivities in H_2. The high inlet velocity (~5 × 10^3 cm/s) at the inlet should also aid mixing within the reaction cell. For a first-order kinetic process the steady-state reactant concentration (C) in a CSTR is given by eq 4, where C^0 is the input concentration, k is the first-order rate constant, and τ is the mean reactor residence time.[47] Rewriting the expression in terms of a product (P) concentration yields eq 5, which we use to analyze the CH_4 and $\rho_w(NH_2)$ IR data.

$$\frac{C}{C^0} = \frac{1}{1 + k\tau} \tag{4}$$

$$\frac{P}{C^0} = \frac{k\tau}{1 + k\tau} \tag{5}$$

By varying temperature and total pressure (P^t) independently, we can perform stringent kinetic tests of the data. Rate constants (k) are typically strong functions of temperature, and the residence time (τ) scales as P^t/T, so we can "decouple" the $k\tau$ product in this manner. Varying P^t is also convenient method of changing initial reactant concentrations. Before using the first-order kinetic expression (eq 5), we need to test for first-order behavior. The $(Me)_3Al{:}NH_3$ adduct is formed very quickly and quantitatively (reaction 1, with equilibrium far to the right), so its initial concentration is determined by the input TMAl concentration. The amount of products are observed to scale linearly with the input TMAl concentration (see Figure 5), consistent with first-order unimolecular decomposition. For the conditions in Figure 5 the reaction conversion was ~20%, which represents a relatively early stage of decomposition. Because NH_3 is in great excess its concentration will not affect the initial $(Me)_3Al{:}NH_3$ concentration, unless the equilibrium in reaction 1 begins to shift back toward the reactants (a possibility at higher temperatures). Bimolecular reaction pathways between NH_3 and $(Me)_3Al{:}NH_3$ have been postulated and studied by theoretical methods,[23,25,27] so it is possible that the reaction kinetics would exhibit an ammonia dependence. Experiments (also at ~20% conversion) varying the NH_3 flow while keeping all other parameters fixed demonstrate a zero-order NH_3 dependence (see Figure 6). These observations support the unimolecular rate law for $(Me)_3Al{:}NH_3$ decomposition, with no evidence of reversibility in reaction 1.

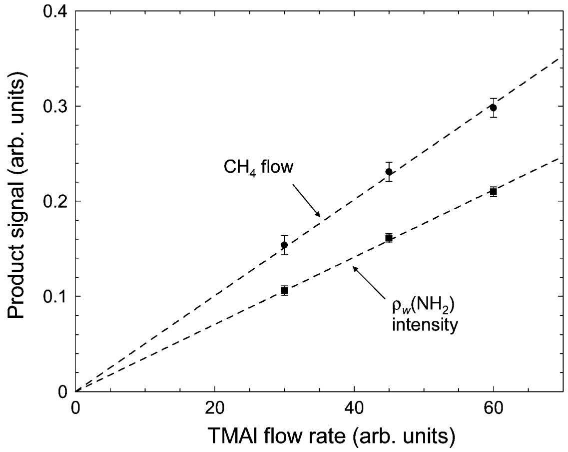

Figure 5. Product concentrations at 437 K, 100 Torr, as function of initial TMAl concentration.

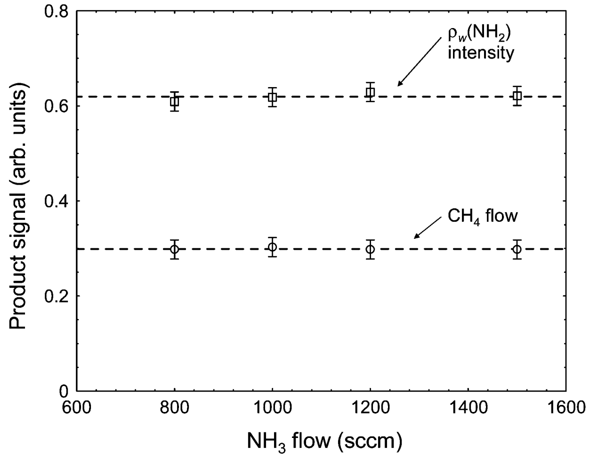

Figure 6. Product concentrations at 437 K, 100 Torr, as function of NH_3 concentration.

Another test for the first-order rate expression (eq 5) can be made by examining the residence time dependence of the reaction kinetics, which we achieve by varying total pressure (recall that $\tau \propto P^t$). Examples of this test are shown in Figure 7, at three intermediate temperatures. The dashed lines are best single parameter fits (k) to eq 5, with k obviously increasing with temperature. The experimental results are obviously well represented by eq 5, which supports the conclusion that $(Me)_3Al{:}NH_3$ obeys first-order decomposition kinetics.

Because all results are consistent with first-order kinetics, we can invert eq 5 and extract the first-order rate constant (k) for all of the data represented in Figures 3 and 4. The results for the CH_4 and $\rho_w(NH_2)$ data sets are shown in Figure 8, with k plotted in Arrhenius fashion. Note that k spans over 3 orders of magnitude and covers a 120 K temperature range. The Arrhenius behavior is quite good, and the best fit parameters are given in Table 2 (uncertainties are $\pm\sigma$). The two experimental methods yield rate constants within 15% of each other

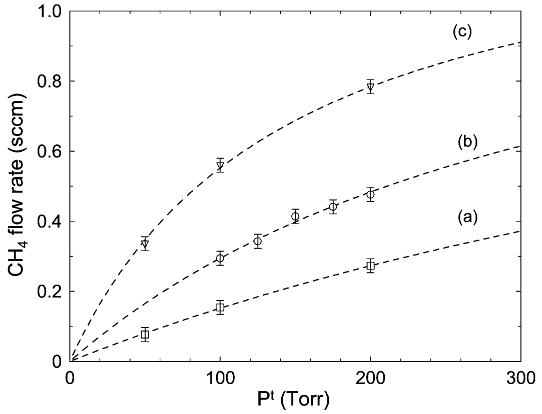

Figure 7. CH_4 production as a function of total pressure (P^t) at (a) 425 K, (b) 436 K, and (c) 451 K. Dashed lines are fits from eq 5 using the residence time ∝ P^t scaling relationship.

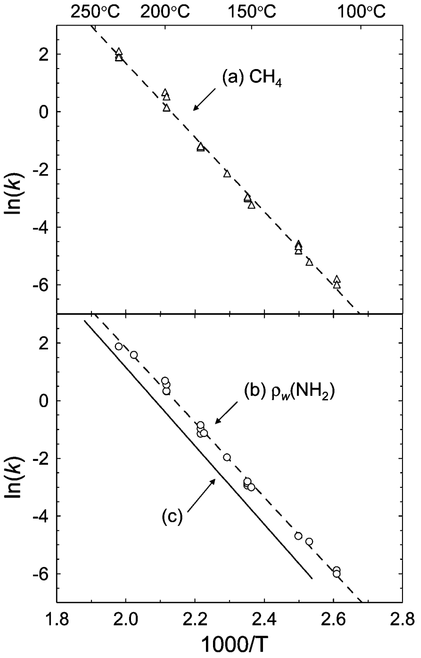

Figure 8. Temperature dependence for the $(Me)_3Al:NH_3$ unimolecular decomposition rate constant: (a, b) this work; (c) theoretical rate constant.[6]

TABLE 2: Arrhenius Parameters for $(Me)_3Al:NH_3$ First-Order Decomposition

param	CH_4	$\rho_w(NH_2)$	theory: ref 6	theory: ref 28
E_a	25.57 ± 0.42	25.73 ± 0.38	27.0	27.3
log(A)	11.91 ± 0.21	12.04 ± 0.19	12.3	not given

over the entire temperature range. Using the Arrhenius expression for k (and the pressure and temperature dependence for τ), we generated the dashed lines in Figures 3 and 4, which is another way to judge the quality of the agreement between the model and experiment. The experimental activation energies are slightly lower than, but generally in very good agreement with, DFT calculations;[6,25,28] see Table 2. The theoretical rate constant of Mihopoulos et al.[6] is shown in Figure 8, curve c, and is within a factor of 3 of our measurements.

As discussed earlier, there is some evidence for a 2nd decomposition step at the highest temperatures that may destroy the dimethylaluminum amide dimer, i.e., $[(Me)_2AlNH_2]_2$, and release more methane. Such a reaction has been noted in condensed phases,[12] and it is often postulated to occur in the MOCVD environment. It is difficult to accurately determine the degree of reaction conversion because of uncertainties in the final CH_4 flow rate and $\rho_w(NH_2)$ absorbance from the first decomposition step. At the highest temperature (574 K) and total pressure (200 Torr) the reaction conversion appears to be in the range of 15 ± 5%. The temperature response of CH_4 and $\rho_w(NH_2)$ absorbance signals imply that the 2nd reaction has a low apparent activation energy (10−14 kcal/mol), but the total pressure behavior does not obey ideal first-order kinetics (eq 4). We have not found conclusive evidence for a 2nd gas-phase $(Me)_xAlNH_y$ product, possibly because of spectral overlap with the dimethylaluminum amide species or low product volatility. The lack of any significant product buildup on the KCl window argues against formation of low volatility product. Unfortunately, the upper temperature limit (~575 K) of this reaction cell prevented us from investigating the 2nd decomposition step in more detail.

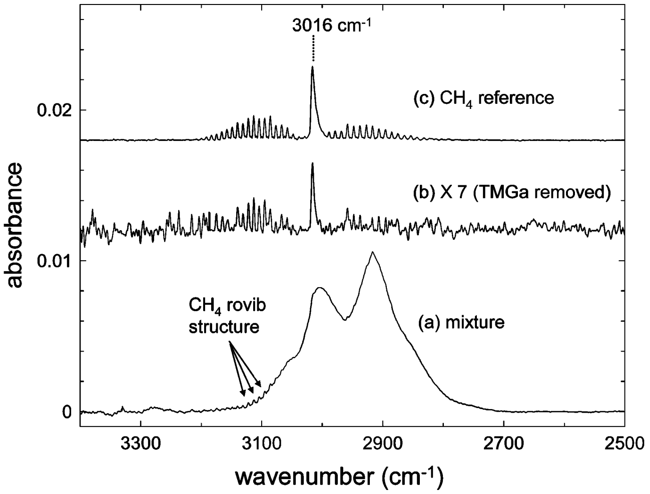

Figure 9. FTIR spectrum in the ν(CH) region of (a) TMGa + NH_3 mixture at 574 K and 200 Torr, NH_3 spectral component removed, (b) curve a with TMGa spectrum removed, intensity scaled ×7, and (c) reference CH_4 at 0.70 sccm.

3.3. Decomposition in TMGa(TMIn) + NH_3 Mixtures. Unlike the TMAl + NH_3 results, heating mixtures of TMGa (or TMIn) and NH_3 does not yield measurable quantities of a $(Me)_2M{-}NH_2$ product over the range of conditions studied. The $(Me)_3M:NH_3$ adducts are readily formed, but for temperatures up to ~543 K, reaction 1 is entirely reversible.[9,13] At the highest temperature studied (574 K) the only gas-phase metalorganic species identified is unassociated (i.e. not bound to NH_3) TMGa (or TMIn). We also find some evidence of an irreversible decomposition reaction(s) that evolve(s) methane. In the case of TMGa + NH_3 mixtures the quantity of CH_4 formed is small and not much above our detection limits. The high-frequency portion of the IR spectrum for a TMGa + NH_3 mixture at 574 K and 200 Torr is shown in Figure 9 (curve a), with the NH_3 component removed. The ν(CH) region from 2800 to 3100 cm^{-1} is virtually identical with the spectrum of pure TMGa taken at lower temperatures, but some small CH_4 rovibrational structure can be seen in the 3100 cm^{-1} region. Removing the TMGa component reveals the 3016 cm^{-1} peak, characteristic of CH_4 (see Figure 9, curve c), that was only seen as a shoulder on the TMGa $\nu(CH_3)$ peak in the original spectrum. By comparing to the CH_4 reference spectrum (Figure 9, curve c), we determine the degree of TMGa decomposition to be 2.4 ± 0.6%. The first-order rate constants at 100 and 200 Torr are given in Table 3 and discussed in more detail in the next section. In addition to the small amount of CH_4 formed at the highest temperature,

TABLE 3: Rate Constants (s^{-1}) for TMGa and TMIn Decomposition Measured by CH_4 Evolution

	const at 574 K, 100 Torr	const at 574 K, 200 Torr
TMGa + NH_3 (+H_2)	0.004 ± 0.002	0.008 ± 0.002
TMIn (+H_2 only)	0.059 ± 0.012	0.067 ± 0.013
TMIn + NH_3 (+H_2)	0.063 ± 0.013	0.035 ± 0.010

there are small intensity peaks at 2250, 2150, and ~910 cm^{-1} that cannot be accounted for by TMGa or $(Me)_3Ga{:}NH_3$. These peaks (particularly the 2150 cm^{-1} peak) appear to belong to a low volatility product that remains on the window (and/or mirror) for a time scale of minutes after the TMGa has been evacuated. We have not yet identified the composition of the product(s) but note that the peaks are not suggestive of the expected $(Me)_2Ga{-}NH_2$ species.

Results for TMIn + NH_3 mixtures at temperatures ≤543 K also exhibit no signs of irreversible decomposition. At 574 K decomposition becomes measurable by CH_4 evolution and occurs at a higher rate than TMGa decomposition. The results, however, are not simple to interpret because even in the absence of NH_3 a significant fraction of the TMIn decomposes to yield CH_4. This is readily apparent in Figure 10, which corresponds to 18 ± 3% TMIn decomposition in H_2 only. The first-order rate constants at 100 and 200 Torr are given in Table 3, and the two values agree within experimental error. The average value is also in good agreement with the experimental values tabulated and reviewed by McDaniel and Allendorf.[48] These authors argue that most, if not all, of the reported TMIn decomposition rates in hot-wall reactors are strongly influenced by heterogeneous effects and that H_2 may play a role in the heterogeneous chemistry. In our current experiment we have no way of ascertaining the relative importance of heterogeneous vs homogeneous chemistry. We do find that the introduction of NH_3 does not increase the decomposition rate and in fact at 200 Torr the rate constant decreases (see Table 3). The observation that NH_3 suppresses CH_4 formation certainly implies that we are not seeing a straightforward reaction sequence described by reactions 1−3. In the TMIn + NH_3 mixtures there are also no clearly identifiable new metal organic species. Given the complexity of the TMIn results (with and without NH_3), we can only put upper limits and boundaries regarding the possible amide reaction rates. Future work using N_2 instead of H_2 carrier gas may shed some light on this complex situation.

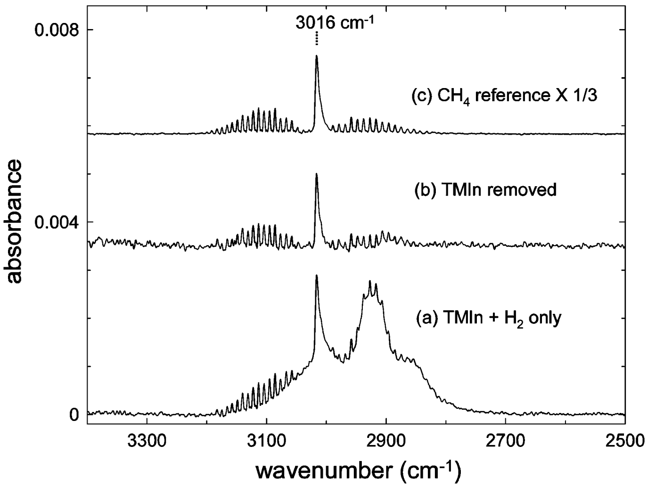

Figure 10. FTIR spectrum in the ν(CH) region of (a) TMIn + H_2 only at 574 K and 200 Torr, (b) curve a with TMIn spectrum removed, and (c) reference CH_4 at 0.70 sccm, intensity scaled ×1/3.

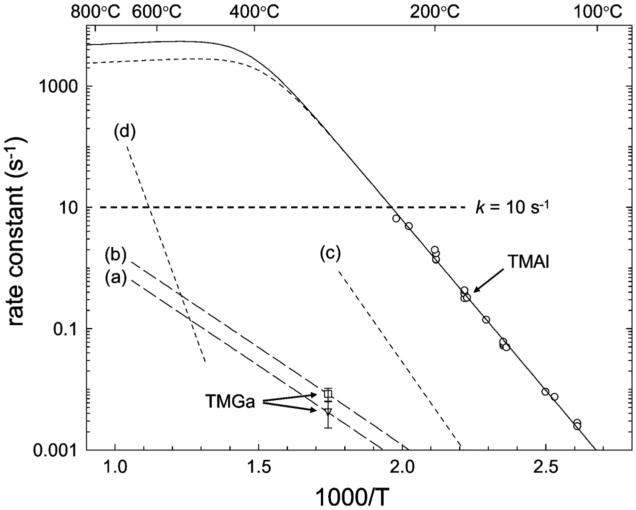

Figure 11. Summary of $TMGa{:}NH_3$ and $TMAl{:}NH_3$ adduct decomposition rate constants, along with simple model predictions that include adduct equilibrium. The two TMGa experimental points are at 100 Torr (triangle) and 200 Torr (square) total pressure. Curves a and b are predictions for k_{eff} (see text) that include adduct equilibrium. Curve c is the estimated k_2 value used for $TMGa{:}NH_3$ reaction 2. Curve d is the rate constant for TMGa pyrolysis.[50] The dashed (100 Torr) and solid (200 Torr) curves through the TMAl data include the effect of adduct equilibrium (estimated) and our measured rate constant (k_2).

3.4. Effect of Adduct Equilibrium on the Decomposition Rate. Finally, we revisit TMGa + NH_3 rate constants in Table 3. Given the nonideal TMIn behavior, it is certainly prudent to view the TMGa measurements with a cautious eye. We do note that TMGa + H_2 mixtures do not produce measurable amounts of CH_4 under the same conditions. And for the TMGa mixtures, doubling the NH_3 concentration (by doubling P^t) doubles the apparent rate constant. This NH_3 dependence is expected because the $(Me_3)_3Ga{:}NH_3$ adduct equilibrium (reaction 1) is shifted far to the reactant side. The expression for the effective first-order rate constant (k_{eff}) for reaction 2 that includes the effect of the equilibrium is given by eq 6, where α is the degree of adduct association and K_p is the equilibrium constant for reaction 1 (expression valid for NH_3 in excess). At low temperatures α ~ 1 and $k_{eff} = k_2$. When $K_pP_{NH_3} \ll 1$ (at high temperatures), the adduct is mostly dissociated ($\alpha \ll 1$) and the rate expression reduces to eq 7:

$$k_{eff} = \alpha k_2 = \frac{k_2}{(1 + (K_pP_{NH_3})^{-1})} \tag{6}$$

$$k_{eff} = k_2K_pP_{NH_3} \tag{7}$$

Under these latter conditions, the original rate constant (k_2) is attenuated by the $K_pP_{NH_3}$ term. At these conditions k_{eff} would exhibit a P_{NH_3} dependence, which is in fact observed for the TMGa results in Table 3 (recall $P_{NH_3} \propto P_t$). This effect is illustrated in Figure 11, where the two experimental TMGa data points are plotted, along with the TMAl results for comparison. To evaluate eq 6 for TMGa, we use the measured K_p curve,[13,49] the known NH_3 partial pressure, and an estimate for k_2. For the $TMGa{:}NH_3$ adduct previous DFT calculations yield an activation energy for reaction 2 in the 30.4−33.8 kcal/mol range.[23,25,27,28] By choosing a value in this range (E_a = 31 kcal/mol), along with a preexponential factor ($\nu = 1 \times 10^{12}$ s^{-1}) identical with our $TMAl{:}NH_3$ measurement (Table 2), we can use eq 6 to quantitatively reproduce the two experimental $TMGa{:}NH_3$ results (see curves a and b in Figure 11). The estimated k_2 is also plotted for comparison (curve c). For the conditions where the TMGa:NH$_3$ measurements were made, k_{eff} is 2−3 orders of magnitude smaller than k_2 due to adduct dissociation. By comparison, the TMGa:NH$_3$ effective decomposition rate constant is also 4−5 orders of magnitude smaller than the TMAl:NH$_3$ rate constant (extrapolated).

In addition to attenuating the absolute rate constant, the effect of the TMGa:NH$_3$ adduct equilibrium also lowers the apparent activation energy by an amount equal to the adduct formation enthalpy, which was measured to be −16.3 kcal/mol.[13,49] So when $\alpha \ll 1$, $E_a = 31 - 16.3 = 14.7$ kcal/mol. This effect moderates the increase in k_{eff} as the temperature is raised and has significant implications for the relative importance of the amide pathway during MOCVD conditions. In most group-III nitride MOCVD systems, the reactor residence times are on the order of seconds, but boundary layer residence times (or time scale gases spend at elevated temperatures) are less, typically no more than tenths of seconds. For a chemical reaction to play a significant role in the overall parasitic reaction scheme, it must have an effective rate constant on the order of $\sim$10 s^{-1} or greater. This model for k_{eff} predicts that temperatures >1000 K are required to reach this level for the NH$_3$ pressures we studied. However, before k_{eff} reaches this magnitude, homogeneous Ga−CH$_3$ bond fission begins to occur at a much faster rate. The rate constant for TMGa → DMGa + CH$_3$, as measured by Jacko and Price,[50] is shown in Figure 11, curve d. The homolysis reaction rate constant approaches $\sim$10 s^{-1} at temperatures just above 873 K and clearly outpaces the adduct decomposition pathway. Significant increases in P_{NH_3} make the amide pathway more viable, but even at atmospheric pressure the radical pathway is more important.

For completeness we apply the model for k_{eff} to the TMAl−NH$_3$ results. In this case we have measured k_2, but K_p must be estimated from theoretical calculations and/or experimental results from related organoaluminum adducts. We used the thermodynamic database compiled by Przhevalskii et al.[51] to extract $\Delta S = -32.6$ eu and $\Delta H = -26.6$ kcal/mol for the (Me$_3$)Al:NH$_3$ equilibrium. The entropy change is similar to what we measure for the TMGa and TMIn adducts,[13] and the stronger dative bond strength (near 27 kcal/mol) is expected.[6,25] The solid (200 Torr) and dashed (100 Torr) curves through the TMAl data in Figure 11 use the estimated K_p parameters and measured k_2 rate constant. In this case the effect of the adduct equilibrium is not apparent until the temperature reaches 673 K, and at that point k_{eff} is >1000 s^{-1}. In this regime the predicted apparent activation energy is nearly zero because of the similarity of E_2 (25.7 kcal/mol) and $-\Delta H$ (26.6 kcal/mol). To keep $k_{eff} < 10$ s^{-1} requires NH$_3$ partial pressures ≤40 mTorr, which is much lower than typically used to grow AlN or AlGaN.

We now review the factors that lead to the substantial differences in the TMAl and TMGa rates for reaction 2. The reaction energies for the two cases are summarized in Figure 12, using the experimental and theoretical values for adduct formation energies and activation energies discussed above. The activation energy for CH$_4$ elimination from the TMGa:NH$_3$ adduct is certainly higher (31 vs 26 kcal/mol), but this effect will only reduce the reaction rate by 1−2 orders of magnitude. This reaction would still be important because the rate will still get large at reasonable temperatues; $k_{eff} \sim 10$ s^{-1} near 673 K. The weaker dative bond in the TMGa adduct (16 vs 27 kcal/mol) is a bigger factor; because it leads to substantial adduct dissociation (reaction 1 reversibility). The TMGa:NH$_3$ adduct equilibrium effect lowers the overall rate another 2−3 orders of magnitude. This reduction in rate is enough to prevent this amide pathway from competing with the *radical* parasitic chemical mechanism under most MOCVD conditions. The importance of the of the dative bond strength was also noted qualitatively by Timoskin and Schaefer.[52]

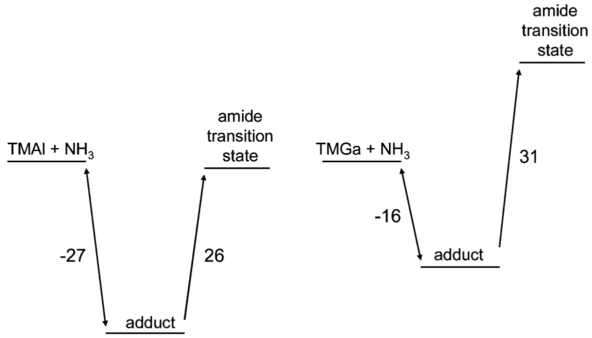

Figure 12. Schematic comparing reaction energies (kcal/mol) for TMAl + NH$_3$ and TMGa + NH$_3$.

4. Summary

Using FTIR we have investigated the early stages of reactivity in TMAl + NH$_3$ (+H$_2$) mixtures at nominal MOCVD input conditions. Near 523 K the TMAl:NH$_3$ decomposes (by reaction 2) quantitatively to yield aminodimethylalane (or dimethylaluminum amide), i.e., (Me$_2$)AlNH$_2$, and CH$_4$. By comparison of the amide IR spectrum with theoretical (DFT) spectra, we conclude that the majority of the gas-phase aluminum amide is dimeric, i.e., [(Me$_2$)AlNH$_2$]$_2$. Kinetics of the adduct decomposition reaction were studied by following the amount of CH$_4$ and amide product formed as a function of temperature, concentration, and reactor residence time. Results demonstrate unimolecular decomposition kinetics with rate constant parameters of $\nu = 1 \times 10^{12}$ s^{-1} and $E_a = 25.7$ kcal/mol (see Table 2). The rate of TMAl:NH$_3$ decomposition is certainly fast enough to participate in the early stages of an *amide* or *concerted* parasitic reaction mechanism for AlN MOCVD. Some evidence of a 2nd decomposition step was found, but the degree of reactivity was not high enough to yield quantitative results.

Except for the very highest temperatures studied, TMGa + NH$_3$ and TMIn + NH$_3$ mixtures are dominated by reversible adduct formation−dissociation (reaction 1) with no CH$_4$ detected. This is due to the much weaker dative bonding in the TMGa:NH$_3$ (16.3 kcal/mol) and TMIn:NH$_3$ (15.0 kcal/mol) adducts, as compared to the TMAl:NH$_3$ adduct ($\sim$27 kcal/mol). At the highest temperature studied (574 K) a small amount of decomposition (1−2%) was observed in TMGa + NH$_3$ mixtures, as evidenced by CH$_4$ formation. The expected gas-phase Ga−amide product was not clearly identified, but some evidence of a low-volatility product was found. The measured TMGa:NH$_3$ rate constants were small, but a simple kinetic model including the effect of adduct equilibrium matched their nominal values and explains the total pressure dependence. This model combines the measured adduct equilibrium constant (K_p) and a decomposition rate constant (k_2) estimated from theoretical and experimental results. Extrapolation of the model to higher temperatures demonstrates that the Ga−amide pathway is still too slow to compete with the radical parasitic chemical mechanism for GaN MOCVD. The reduced rate of TMGa:NH$_3$ decomposition can mainly be traced to the effect of the weaker dative bonding (as compared to TMAl:NH$_3$). At 574 K we also begin to see CH$_4$ formation in TMIn + NH$_3$ mixtures. However, a background TMIn decomposition pathway that does not involve NH$_3$ masks possible TMIn:NH$_3$ decomposition.

We can therefore only put an upper limit on the TMIn:NH_3 decomposition rate. On the basis of the known TMIn:NH_3 equilibrium constant[13] and estimated values for k_2, we expect decomposition rates in the same range as the TMGa:NH_3 values.

Acknowledgment. We thank Dan Koleske for a critical reading of this manuscript and T. M. Kerley and M. J. Russell for technical assistance. J.R.C. also thanks M. E. Bartram for his scientific expertise during the early stages of this study. Sandia is a multiprogram laboratory operated by Sandia Corp., a Lockheed Martin Co. for the U.S. Department of Energy's National Nuclear Security Administration under Contract No. DE-AC04-94AL85000. We especially acknowledge support from the Office of Basic Energy Sciences.

References and Notes

(1) Neumayer, D.; Ekerdt, J. G. *Chem. Mater.* **1996**, *8*, 10.

(2) Han, J.; Figiel, J. J.; Crawford, M. H.; Banas M. A.; Bartram, M. E.; Biefeld, R. M.; Song, Y. K.; Nurmikko, A. V. *J. Cryst. Growth* **1998**, *195*, 291.

(3) Sayyah K.; Chung, B.-C.; Gershenzon, M. *J. Cryst. Growth* **1986**, *77*, 424.

(4) Chen C. H.; Liu, H.; Steigerwald, D.; Imler, W.; Kuo, C. P.; Craford, M. G.; Ludowise, M.; Lester, S.; Amano, J. *J. Electron. Mater.* **1996**, *25*, 1004.

(5) Nakamura, F.; Hashimoto, S.; Hara, M.; Imanaga, S.; Ikeda, M.; Kawai, H. *J. Cryst. Growth* **1998**, *195*, 280.

(6) Mihopoulos, T. G.; Gupta, V.; Jensen, K. F *J. Cryst. Growth* **1998**, *195*, 733.

(7) Creighton J. R.; Coltrin, M. E.; Breiland, W. G. *ECS Proc.* **2002−2003**, 28−35.

(8) Creighton, J. R.; Breiland, W. G.; Coltrin, M. E.; Pawlowski R. P. *Appl. Phys. Lett.* **2002**, *81*, 2626.

(9) Creighton, J. R.; Wang, G. T.; Breiland, W. G.; Coltrin, M. E. *J. Cryst. Growth* **2004**, *261*, 204.

(10) Safvi S. A.; Redwing, J. M.; Tischler, M. A.; Kuech, T. F. *J. Electrochem. Soc.* **1997**, *144*, 1789

(11) Creighton, J. R. *J. Electron. Mater*. **2002**, *31*, 1337.

(12) Sauls, F. C.; Interrante, L. V. *Coord. Chem. Rev.* **1993**, *128*, 193.

(13) Creighton, J. R.; Wang, G. T. *J. Phys. Chem. A* **2005**, *109*, 136.

(14) Coates, G. E. *J. Chem. Soc*. **1951**, 2003.

(15) Almond, M. J.; Drew, M. G. B.; Jenkins, C. E.; Rice, D. A. *J. Chem. Soc., Dalton Trans.* **1995**, 5.

(16) Sauls, F. C.; Interrante, L. V.; Jiang Z. *Inorg. Chem.* **1990**, *29*, 2990.

(17) Thon A.; Kuech T. F. *Appl. Phys. Lett.* **1996**, *69*, 55.

(18) Schäfer, J.; Simmons, A.; Wolfrum, J.; Fischer, R. A. *Chem. Phys. Lett*. **2000**, *319*, 477.

(19) Bergman, U.; Reimer, V.; Atakan, B. *Phys. Status Solidi a* **1999**, *176*, 719.

(20) Sywe, B. S.; Schlup, J. R.; Edgar, J. H. *Chem. Mater*. **1991**, *3*, 737.

(21) Almond, M. J.; Jenkins, C. E.; Rice, D. A.; Hagen, K. *J. Organomet. Chem*. **1992**, *439*, 251.

(22) Kim, S. H.; Kim, H. S.; Hwang, J. S.; Choi, J. G.; Chong, P. J. *Chem. Mater*. **1994**, *6*, 278.

(23) Simka, H.; Willis, B. G.; Lengyel, I.; Jensen, K. F. *Prog. Cryst. Growth Charact.* **1997**, *2−4*, 117.

(24) Makino, O.; Nakamura, K.; Tachibana, A.; Tokunaga H.; Akutsu, N.; Matsumoto, K. *Appl. Surface Sci*. **2000**, *159−160*, 374.

(25) Nakamura, K.; Makino, O.; Tachibana, A.; Matsumoto, K. *J. Organomet. Chem*. **2000**, *611*, 514.

(26) Timoshkin, A. Y.; Bettinger, H. F.; Schaefer, H. F., III. *J. Phys. Chem*. **2001**, *105*, 3240.

(27) Watwe, R. M.; Dumesic, J. A.; Kuech, T. F. *J. Cryst. Growth* **2000**, *221*, 751.

(28) Ikenaga, M.; Nakamura, K.; Tachibana, A.; Matsumoto, K. *J. Cryst. Growth* **2002**, *237−239*, 936.

(29) Sengupta D. *J. Phys. Chem. B* **2003,** *107*, 291.

(30) Stringfellow, G. B. *Organometallic Vapor-Phase Epitaxy*, 2nd ed.; Academic Press: San Diego, CA, 1999; Table 4.5.

(31) Plass, C.; Heinecke, H.; Kayser, O.; Lüth, H.; Balk, P. *J. Cryst. Growth* **1988**, *88*, 455.

(32) Kayser, O.; Heinecke, H.; Brauers, A.; Lüth, H.; Balk, P. *Chemtronics* **1988**, *3*, 90.

(33) Becke, A. D. *J. Chem. Phys.* **1993**, *98*, 5648.

(34) Frisch, M. J.; Trucks, G. W.; Schlegel, H. B.; Scuseria, G. E.; Robb, M. A.; Cheeseman, J. R.; Montgomery, J. A., Jr.; Vreven, T.; Kudin, K. N.; Burant, J. C.; Millam, J. M.; Iyengar, S. S.; Tomasi, J.; Barone, V.; Mennucci, B.; Cossi, M.; Scalmani, G.; Rega, N.; Petersson, G. A.; Nakatsuji, H.; Hada, M.; Ehara, M.; Toyota, K.; Fukuda, R.; Hasegawa, J.; Ishida, M.; Nakajima, T.; Honda, Y.; Kitao, O.; Nakai, H.; Klene, M.; Li, X.; Knox, J. E.; Hratchian, H. P.; Cross, J. B.; Adamo, C.; Jaramillo, J.; Gomperts, R.; Stratmann, R. E.; Yazyev, O.; Austin, A. J.; Cammi, R.; Pomelli, C.; Ochterski, J. W.; Ayala, P. Y.; Morokuma, K.; Voth, G. A.; Salvador, P.; Dannenberg, J. J.; Zakrzewski, V. G.; Dapprich, S.; Daniels, A. D.; Strain, M. C.; Farkas, O.; Malick, D. K.; Rabuck, A. D.; Raghavachari, K.; Foresman, J. B.; Ortiz, J. V.; Cui, Q.; Baboul, A. G.; Clifford, S.; Cioslowski, J.; Stefanov, B. B.; Liu, G.; Liashenko, A.; Piskorz, P.; Komaromi, I.; Martin, R. L.; Fox, D. J.; Keith, T.; Al-Laham, M. A.; Peng, C. Y.; Nanayakkara, A.; Challacombe, M.; Gill, P. M. W.; Johnson, B.; Chen, W.; Wong, M. W.; Gonzalez, C.; Pople, J. A. *Gaussian 03*; Gaussian, Inc.: Pittsburgh, PA, 2003.

(35) Scott, A. P.; Radom, L. *J. Phys. Chem.* **1996**, *100*, 16502.

(36) Wang, G. T.; Creighton, J. R. Submitted for publication in *J. Phys. Chem. A*.

(37) Ault, B. S. *J. Phys. Chem*. **1992**, *96*, 7908.

(38) Müller, J. *J. Am. Chem. Soc*. **1996**, *118*, 6370

(39) Haaland, A. *Angew. Chem., Int. Ed. Engl.* **1989**, *28*, 992.

(40) Alford, K. J.; Gosling, A. K.; Smith, J. D. *J. Chem. Soc., Dalton Trans.* **1972**, 2203.

(41) Müller, J.; Margiolis, K.; Dehnicke, K. *J. Organomet. Chem*. **1972**, *46*, 219.

(42) Gerstner, F.; Schwarz, W.; Hausen, H.-D.; Weilden, J. *J. Organomet. Chem*. **1979**, *175*, 33.

(43) Ouzounis, V. K.; Riffel, H.; Hess, H.; Kohler, U.; Weidlein, J. *Z. Anorg. Allg. Chem.* **1983**, *504*, 67.

(44) Hall, R. E.; Schram, E. P. *Inorg. Chem.* **1969**, *8*, 270.

(45) Jacox, M. E. *Chem. Soc. Rev.* **2002**, *31*, 108.

(46) Timoshkin, A. Y.; Bettinger, H. F.; Schaefer, H. F., III. *J. Am. Chem. Soc*. **1997**, *119*, 5668.

(47) Hill, C. G., Jr., *An Introduction to Chemical Engineering & Reactor Design*; John Wiley: New York, 1977; Chapter 8.

(48) McDaniel, A. H.; Allendorf, M. D. *Chem. Mater.* **2000**, *12*, 450.

(49) Pelekh A.; Carr, R. W. *J. Phys. Chem. A* **2001**, *105*, 4697.

(50) Jacko, M. G.; Price, S. J. W. *Can. J. Chem*. **1964**, *41*, 1560.

(51) Przhevalskii, I. N.; Karpov, S. Y.; Makarov, Y. N. *MRS Int. J. Nitride Semicond. Res.* **1998**, *3*, 30.

(52) Timoshkin, A. Y.; Schaefer, H. F., III. *Chem. Rec.* **2002**, *2*, 319.